ARTICLE NO. 79-0203R

J80-012

Transonic Wind Tunnel Interference Assessment—Axisymmetric Flows

20005
20018

Stephen S. Stahara*
Nielsen Engineering & Research, Inc., Mountain View, Calif.
and
John R. Spreiter†
Stanford University, Stanford, Calif.

A wind tunnel interference assessment concept that presents a rational predictive means of wall interference analysis is evaluated. The procedure consists of employing as an outer boundary condition an experimentally measured pressure distribution along a convenient control surface located inward from the actual tunnel walls. Attention has been focused on axisymmetric flows in the transonic regime, where tunnel interference is high and where the experimentally measured conditions on the control surface are of mixed subsonic/supersonic type. Based on the transonic small-disturbance equation, results for surface and near-flow field pressure distributions are presented for a variety of different slender-body shapes. These calculations indicate both the accuracy of the procedure as well as its ease of implementation. The procedure relates directly to the correctable-interference wind-tunnel concept recently suggested.

Introduction

THE assessment of transonic wind-tunnel interference remains an unsatisfactorily resolved problem after almost three decades use of the ventilated tunnel wall concept. The classical homogeneous wall boundary conditions[1] for modeling perforated or porous and slotted walls have proven to be of considerable value for providing insight into the overall effects of ventilated tunnel walls at transonic speeds,[2,3] but as presently constituted, they are seriously deficient for a quantitative study of wall interference. Although the wall characteristics are known to depend on geometrical (test article, tunnel ventilation geometry) as well as flow parameters (M_∞, Re, local blowing pressure), the exact nature of the wall flow is not adequately known. It has been widely assumed that it is basically viscous in character,[4] although some recent slotted-wall results by Berndt[5] indicate that, under certain conditions, the wall flow for slotted walls may not be completely dominated by viscosity. For porous walls, it has been found[6,7] that the wall boundary layer can create a nonlinear relationship between velocity normal to the wall and the difference in pressure across the wall. Kacprzynski[8] has demonstrated the feasibility of two-dimensional potential flow calculations using an assumed nonlinear wall characteristic. The present state of development, however, of ventilated-wall boundary conditions is such that they are inadequate as a predictive method; namely, they cannot provide a quantitative a priori assessment of tunnel interference at transonic speeds.

The adaptive-wall concept[9-13] is an attempt to remedy this situation by combining an interference-assessment capability together with a tunnel-wall modification capability to actually eliminate the interference. Notwithstanding the problems associated with the implementation of adaptive-wall technology, the fact remains that many of the currently operating transonic tunnels possess only a limited degree of wall control or none at all. Consequently, the concept of a correctable-interference transonic tunnel recently proposed,[14] and toward which the procedures described in this paper are related, appears to have strong merit. The heart of the correctable-interference concept is that the distribution of a single experimentally measured flow quantity (e.g., pressure or flow angle), obtained along a convenient control surface located sufficiently inward from the actual tunnel walls so as to be removed from local wall disturbances, is employed as an outer boundary condition. This, together with several additional constraints, is used with a calculative procedure to determine the potential flow interior to the control surface. That tunnel-flow solution, in turn, provides the basis for a corresponding free-air calculation, which then determines a quantitative correction for tunnel-interference effects.

In this paper we formulate the assessment procedure based on a measured pressure-distribution outer-boundary condition and an inviscid body boundary condition, describe its application to axisymmetric transonic flows past a variety of slender bodies, and demonstrate its effectiveness by extensive comparisons with data. The theoretical predictions employ finite-difference successive line over-relaxation (SLOR) solutions of the axisymmetric transonic small-disturbance potential equation. Results are presented for pressure distributions on the surface and in the near flowfield of these various slender bodies at freestream Mach numbers throughout the transonic regime. In order to provide a severe test of the procedure, the particular geometries and flow conditions were purposely selected to be in a range of freestream Mach numbers near one, where the tunnel interference is most pronounced, and where the experimentally measured data on the control surface are of mixed subsonic/supersonic character.

Analysis

Basic Equations

The coordinate system employed in the analysis is a body-fixed cylindrical system with origin at the nose of the body as illustrated in Fig. 1. The flow is assumed to be inviscid and steady, and the body shapes sufficiently slender and smooth

Presented as Paper 79-0203 at the AIAA 17th Aerospace Sciences Meeting, New Orleans, La., Jan. 15-17, 1979; submitted Feb. 8, 1979; revision received June 28, 1979.

Index categories: Transonic Flow; Computational Methods.

*Senior Research Scientist, Engineering Management. Member AIAA.

†Professor, Division of Applied Mechanics; Consultant to Nielsen Engineering & Research, Inc. Fellow AIAA.

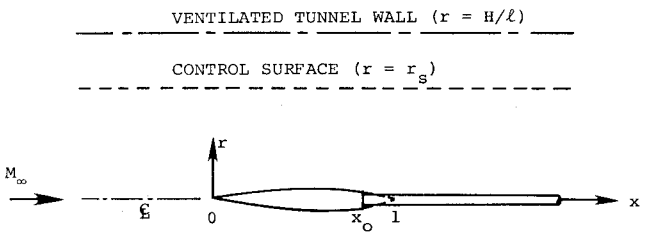

Fig. 1 Illustration of model and tunnel geometry.

that the resulting flowfield is irrotational and adequately treated by small-disturbance theory. Accordingly, a disturbance velocity potential ϕ can be defined by

$$\Phi(x,r) = U_\infty \ell[x+\phi(x,r)] \tag{1}$$

where Φ is the total velocity potential, U_∞ represents the uniform oncoming velocity, ℓ is the complete body length, and the coordinates (x,r) have been nondimensionalized by ℓ. The governing partial-differential equation for ϕ is the usual axisymmetric transonic small-disturbance equation

$$[(1-M_\infty^2)\phi_x - 1/2M_\infty^2(\gamma+1)\phi_x^2]_x + (1/r)(r\phi_r)_r = 0 \tag{2}$$

The pressure coefficient in the vicinity of the slender body is given by

$$C_p(x,r) = -2\phi_x(x,r) - \phi_r^2(x,r) \tag{3}$$

With regard to the flow domain indicated in Fig. 1, the boundary conditions to be imposed on the solution consist of: 1) outer flow conditions on the upstream, downstream, and lateral boundaries which are appropriate to the behavior of the body in a free-air or wind-tunnel environment; 2) the body surface condition of no normal flow; and 3) shock wave conditions to be applied at any shock surface appearing in the flow, such that the potential is continuous through the shock and the velocity components satisfy the small-disturbance approximation to the Rankine-Hugoniot conditions at the location of the shock. The appropriate outer flow boundary conditions are discussed in the following section. The requirements on the body and shock surface lead to the following conditions on ϕ

$$\lim_{r\to 0}(r\phi_r) = S'(x)/2\pi \tag{4}$$

$$[\![\phi]\!]_{\text{shock}} = 0; \quad \{r[1-M_\infty^2 - M_\infty^2(\gamma+1)\langle\phi_x\rangle] \cdot [\![\phi_x^2]\!] + [\![(r\phi_r)^2]\!]\}_{\text{shock}} = 0 \tag{5}$$

where $S(x)$ is the body cross-sectional area distribution nondimensionalized by ℓ^2, and the symbols $[\![\ ]\!]$ and $\langle\ \rangle$ signify the difference and the mean, respectively, of the enclosed quantity on the two sides of the shock surface.

Outer Boundary Conditions

The outer boundary condition to be applied along the cylindrical control surface indicated in Fig. 1 is determined from static pressure measurements. The actual condition imposed on ϕ is of Dirichlet type and is given by

$$\phi(x,r_s) = -\tfrac{1}{2}\int_{x_1}^{x} C_{pm}(\xi,r_s)\,d\xi + \phi(x_1,r_s) \tag{6}$$

where r_s denotes the radial location of the control surface, x_1 the position of the upstream boundary, and C_{pm} the measured pressure coefficient along r_s. The quantity $\phi(x_1,r_s)$, which is proportional (to within a constant) to the average flow inclination at the upstream boundary, has for convenience and

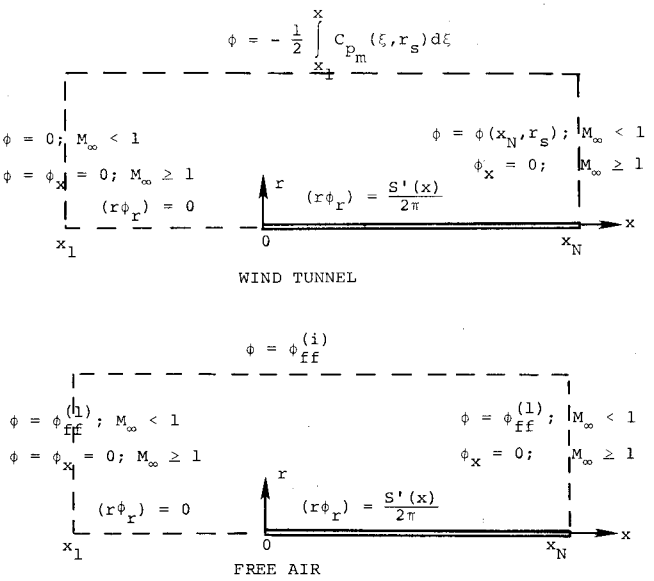

Fig. 2 Summary of boundary conditions for free-air and wind-tunnel environment.

without loss of generality been set to zero. Along the upstream and downstream boundaries for subsonic oncoming flow, we have employed the conditions

$$M_\infty < 1: \quad \phi(x_1,r) = 0; \quad \phi(x_N,r) = \phi(x_N,r_s) \tag{7}$$

while for sonic and supersonic oncoming flow, we have used the uniform flow conditions

$$M_\infty \geq 1: \quad \phi(x_1,r) = \phi_x(x_1,r) = 0; \quad \phi_x(x_N,r) = 0 \tag{8}$$

while, strictly speaking, for $M_\infty > 1$, no condition is required at the downstream boundary if, as we assume, it is sufficiently far removed so that the outflow is entirely supersonic. For actual numerical application, however, some condition is needed[3] to treat subsonic outflow which may develop during the course of the relaxation solution process prior to convergence. From numerical experimentation, the condition $\phi_x = 0$ given in Eq. (8) has been found to be satisfactory. These conditions are summarized in Fig. 2.

For the corresponding comparative free-air calculations, we have employed the following conditions. For $M_\infty < 1$ flows, the asymptotic far-field solution ϕ_{ff} given by an axisymmetric source and axisymmetric doublet[15] is employed on all the outer boundaries, i.e.,

$$\phi_{ff}^{(1)}(x,r) = \frac{-S_0}{2\bar{r}} + \tfrac{1}{4}\left[-S_0 + 2\int_0^{x_0} S(\xi)\,d\xi + M_\infty^2(\gamma+1)\int_{-\infty}^{\infty}\int_0^{\infty}\phi_x^2(\xi,r)\,r\,dr\,d\xi\right]\cdot\frac{\bar{x}}{\bar{r}^3} \tag{9}$$

where $\bar{r} = [\bar{x}^2 + (1-M_\infty^2)r^2]^{1/2}$, $\bar{x} = x - 1/2$, x_0 is the location of the body base, and S_0 is either the base area of the body or that of a sting attached to the body base nondimensionalized by ℓ^2. On the lateral boundary, for $M_\infty = 1$ flows, we employ the asymptotic solution behavior[16]

$$\phi_{ff}^{(2)}(x,r) = \frac{f(x/r^{4/7})}{r^{2/7}} \tag{10}$$

while for $M_\infty > 1$, the following relation[17] is used:

$$\phi_{ff}^{(3)}(x,r) = g\left[x - \sqrt{M_\infty^2 - 1}\,r - \frac{M_\infty^2(\gamma+1)\cdot r\phi_x}{\sqrt{M_\infty^2-1}}\right]\Big/\sqrt{r} \tag{11}$$

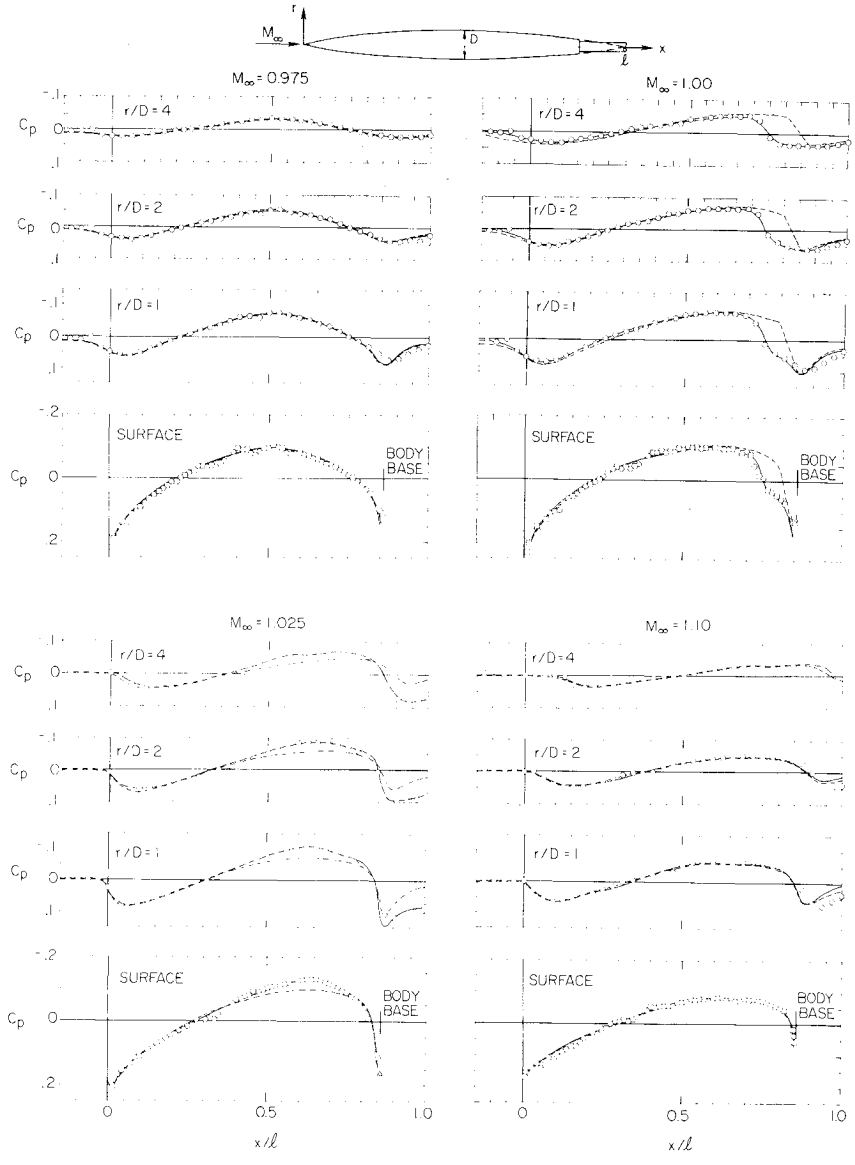

Fig. 3 Experimental[20] (○, □) and theoretical (——) pressure distributions for a parabolic-arc body with $D/\ell = 1/12$ at several transonic Mach numbers; —C_{pm} ($r/D = 4$) input, --- free air.

The conditions given by Eqs. (10) and (11) are implemented in the following way. For Eq. (10), along lines of $x/r^{4/7} = \text{const}$, we have $r^{2/7} \cdot \phi_{ff}^{(2)} = \text{const}$. By using values of $\phi^{(2)}$ from a previous iteration along the grid row just interior to the outer boundary, the value of $\phi_{ff}^{(2)}$ along the outer boundary is then determined by: 1) following lines of $x/r^{4/7} = \text{const}$ from that interior grid row to the outer boundary, and 2) calculating $\phi_{ff}^{(2)}$ at those locations from the relation $(r^{2/7} \cdot \phi_{ff}^{(2)})_{\text{boundary}} = (r^{2/7} \cdot \phi^{(2)})_{\text{interior}}$. An analogous procedure is employed for Eq. (11). On the upstream and downstream boundaries, for $M_\infty \geq 1$, the conditions given in Eq. (8) are employed. All these conditions are also summarized in Fig. 2.

Computational Procedure

The method employed for the solution of Eq. (2) is a finite-difference SLOR procedure using Murman-Cole type-dependent difference operators.[18] To realize the calculation, we have employed the following fully conservative form

$$[\eta(K\bar{\phi}_x - \tfrac{1}{2}\bar{\phi}_x^2)]_x + [\eta\bar{\phi}_\eta]_\eta = 0 \tag{12}$$

where

$$\bar{\phi}(x,\eta) = \phi(x,r)/\tau^2; \quad K = (1 - M_\infty^2)/\tau^2 M_\infty^2 (\gamma + 1);$$

$$\eta = \tau M_\infty \sqrt{\gamma + 1}\, r \tag{13}$$

and τ denotes the thickness ratio of the body. The finite-difference form of the equation actually solved is that suggested by Jameson[19] in terms of a correction potential. Additionally, a pseudotime term of the form $-\epsilon(\Delta t/\Delta x)\phi_{xt}$ was added to enhance stability and speed convergence.

Results

In order to examine the feasibility of the procedure just described for assessing tunnel interference, as well as to examine the stability and convergence characteristics of the computational method subject to the experimentally imposed Dirichlet condition of Eq. (6), we have tested the method extensively using data obtained in a conventional transonic tunnel on five different slender-body shapes and at Mach numbers at and near one. The particular geometries and flow conditions were purposely selected to study situations where tunnel interference is most pronounced, and insofar as possible where the experimentally-measured data on the control surface are of mixed subsonic/supersonic character.

The body shapes examined are: 1) parabolic-arc,[20] 2) power-law body with $S_{\max}$ at $x = 0.3$,[20] 3) power-law body with $S_{\max}$ at $x = 0.7$,[20] 4) parabolic-arc with bumpy midsection,[21] and 5) parabolic-arc with indented midsection.[21] Data for all these bodies were obtained in the Ames 14-ft transonic wind tunnel.

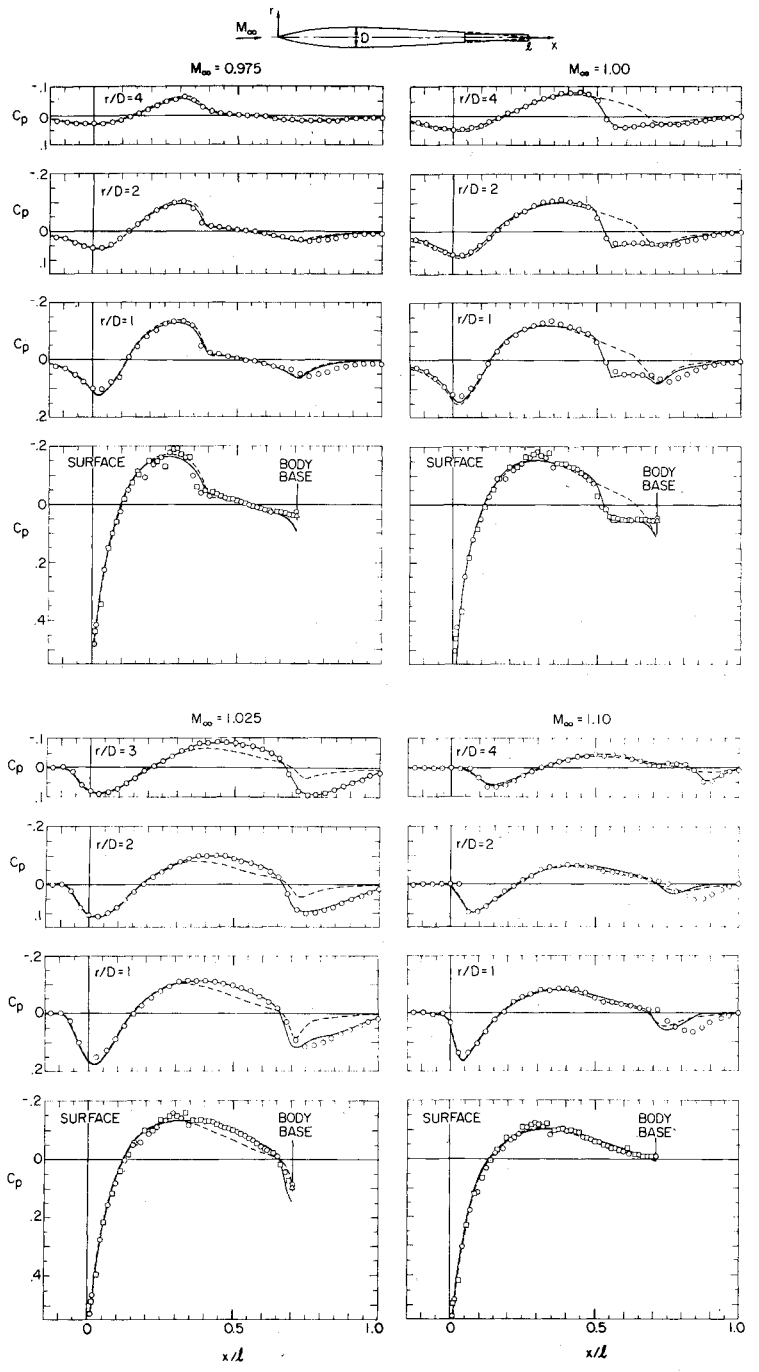

Fig. 4 Experimental[20] (○, □) and theoretical (-----) pressure distributions for a body with maximum thickness at $x/\ell = 0.3$ and $D/\ell = 1/12$ at several transonic Mach numbers: —C_{p_m} ($r/D = 4$) input, --- free air.

Smooth Bodies

In Figs. 3-5, we have displayed comparisons of theoretical results with data[20] for the three smooth body shapes described above. In these results, the theoretical body surface pressure coefficients were determined by extrapolating the SLOR results obtained along the first radial grid line r_1 down to the body surface according to the slender-body result

$$C_p(x,R) = -\left[2\phi_x(x,r_1) + \frac{S''(x)}{\pi}\ln\left(\frac{R}{r_1}\right) + \left(\frac{dR}{dx}\right)^2\right] \quad (14)$$

where R is the body radius. The flowfield pressures were calculated by bilinear interpolation for ϕ through the flowfield grid, then employing Eq. (3) to calculate the pressure coefficient. The (x,r) mesh density used for the imposed pressure-distribution calculations was (80×24) with 40 equally-spaced points on the body. The r-grid as well as the x-grid ahead and behind the body were expanded geometrically using a grid ratio of 1.2:1. The x-mesh extended two body lengths ahead and two body lengths behind the body. The location of the first r-grid line was at $r = D/2\ell$ and the control surface was at $r_s = 1/3$. For the free-air calculations, an identical x-mesh was used and a 40-point r-grid was employed that was identical to the previous r-mesh out to $r = 1/3$, but which was continued laterally out to $r = 5$. In numerically implementing the imposed pressure-distribution boundary condition, Eq. (6), it was necessary to extend the data[20,21] to the upstream and downstream boundaries, since the experimental pressures were only obtained for $-0.15 \sim x/\ell < 1.0$. This was accomplished by linearly extrapolating the flowfield pressure distributions from the last experimental values obtained ahead and behind the body to a freestream value of zero C_p at the upstream and downstream boundaries. In addition, numerical experimentation indicated that some degree of data point smoothing was desirable. Because the data sometimes con-

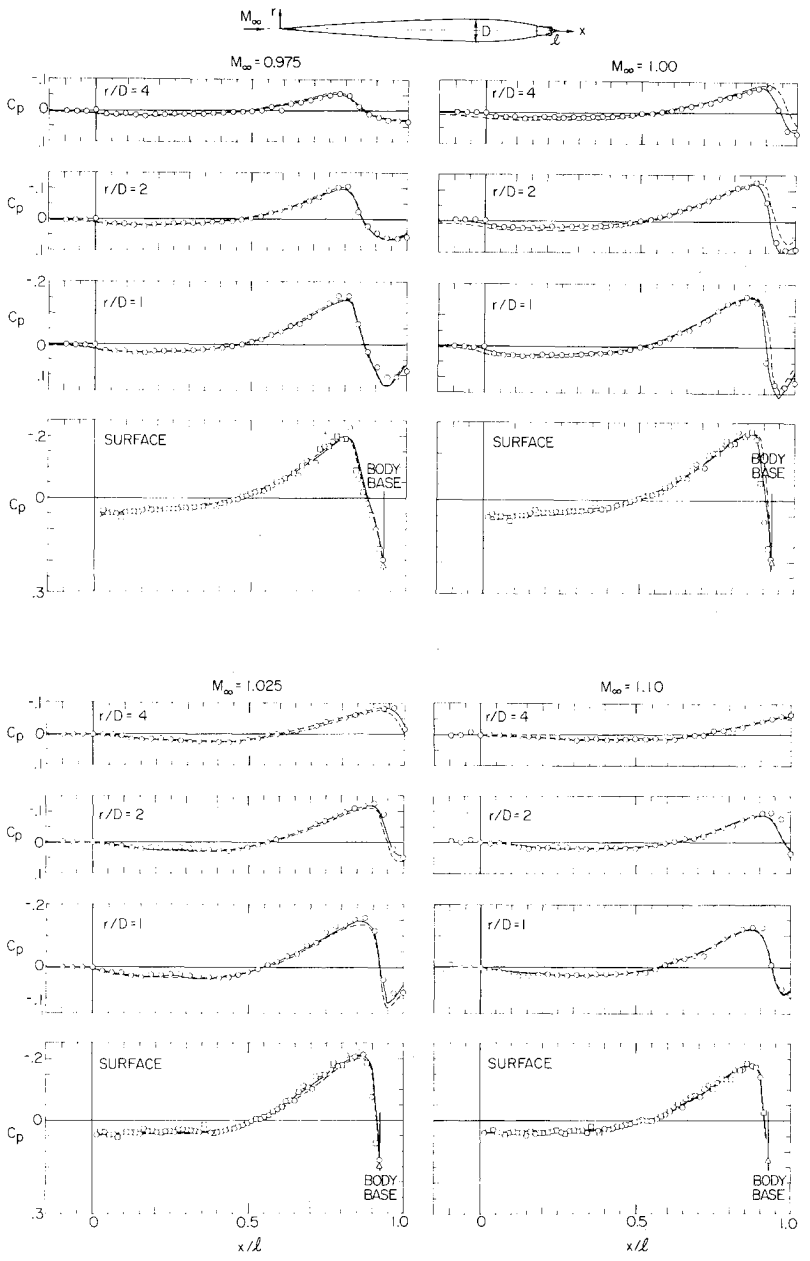

Fig. 5 Experimental[20] (○, □), and theoretical (-----) pressure distributions for a body with maximum thickness at $x/\ell = 0.7$ and $D/\ell = 1/12$ at several transonic Mach numbers; — C_{p_m} $(r/D = 4)$ input, --- free air.

tained one or more shock waves, however, and the faithful reproduction of those shock profiles was considered essential, the method selected was a least-squares smoothing spline fit with individual-point weighing. As can be seen in Fig. 3, as well as in the results to follow, this produced extremely satisfactory results in all cases considered. In the SLOR solution process, relaxation factors $1.7 < \omega < 1.9$ were used and the coefficient of the pseudotime term was set to $\epsilon = 0.5$. No stability problems were encountered and convergence in all of the imposed pressure-distribution cases was very rapid, with a $|\Delta\phi|_{max} < 10^{-5}$ criteria reached within 75 iteration sweeps. Pressure changes on the body usually become less than 10^{-4} before 40 iterations. The corresponding results for the free-air calculations generally required about 25% more iteration cycles to reach the same convergence level.

In Fig. 3 we have displayed comparisons of the theoretical results with data[20] for a parabolic-arc body of revolution having a diameter to complete body length $D/\ell = 1/12$. Results are shown at freestream Mach numbers $M_\infty = 0.975$, 1.00, 1.025, and 1.10. For the particular body tested, the tunnel half-height to complete body length ratio was $H/\ell = 7/6$. The theoretical results indicated by the solid lines represent SLOR solutions of Eq. (12) employing the measured pressure-distribution outer boundary condition, Eq. (6). Pressure-survey data obtained at the radial location $r/D = 4$, which represents the outermost survey station at which data were taken, were used. The results indicated by the dashed lines represent the corresponding theoretical results for free-air conditions, Eqs. (9-11).

With regard to the comparisons, we note that the agreement between the data and the imposed pressure-condition theoretical results is excellent for both surface and flowfield pressures. The location and strengths of shocks are accurately predicted throughout this flow-sensitive Mach number range. Viscous effects on these flows, which have Reynolds numbers based on a body length of approximately 24 million, appear to be quite small and confined to the flow immediately behind the body base where the stepdown sting results in a separated flow situation. Reported[20,21] accuracy of the experimental measurements is that the freestream Mach numbers are repeatable to within ± 0.002 and the pressure-coefficient data to within ± 0.005. The corresponding theoretical free-air results are interesting in that they indicate essentially no tunnel interference at $M_\infty = 0.975$, a substantial amount at $M_\infty = 1.00$ and 1.025, and then very little again at $M_\infty = 1.10$. This serves to point out the narrowness of the critical range

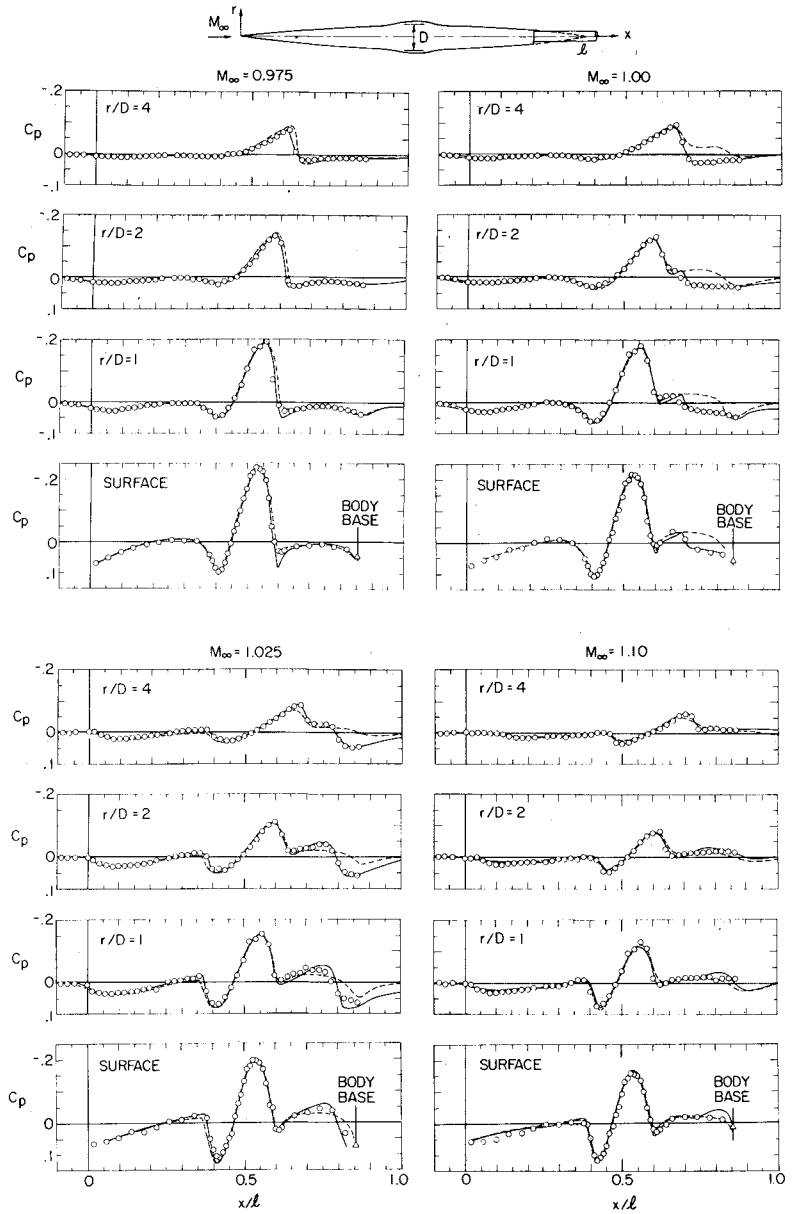

Fig. 6 Experimental[21] (○, □), and theoretical (-----) pressure distributions for a bumpy parabolic-arc with $D/\ell = 1/14$ at several transonic Mach numbers; —— C_{pm} $(r/D = 4)$ input, --- free air.

for this class of smooth, slender bodies.

Figure 4 presents analogous results for a slender body having the same maximum diameter to length ratio $(D/\ell = 1/12)$ as the parabolic-arc body of Fig. 3, but with the location of maximum diameter at 30% of the body length. The ordinates of this body are given by

$$R = A[(1-x) - (1-x)^n] \tag{15}$$

where $n = 6.03$ and A is related to D/ℓ and n by

$$A = [n^{n/(n-1)}/2(n-1)](D/\ell) \tag{16}$$

As in the case of the parabolic-arc body, comparisons of the C_{pm}-input theoretical results with data again display excellent agreement. The corresponding free-air comparisons indicate that the tunnel-interference effects are more pronounced for this shape than for the parabolic-arc. This is to be anticipated and is in accord with the observations noted in Ref. 22 that, for a given thickness ratio and length, wave reflection interference on the afterbody region increases as the point of maximum thickness moves forward.

We note for this body that the $M_\infty = 0.975$ results display only slight interference, while the $M_\infty = 1.00$ comparisons indicate strong tunnel interference which has resulted in a shock movement on the body surface of approximately 15% of the body length. For the $M_\infty = 1.025$ results, the measured boundary condition was imposed at $r/D = 3$ rather than 4, since $r/D = 4$ data were not obtained for this flow. We observe that the comparison of the predicted result with data is quite good, in particular, even for the flowfield pressures at x locations behind the body base. Only for the $M_\infty = 1.10$ case does a slight discrepancy arise, and that only for the flowfield results at locations behind the body base. This may be caused by the interaction of an oblique shock emanating from the body base and interacting with the separated base flow. A more modest indication of this can be observed in the corresponding results at $M_\infty = 1.10$ for the parabolic-arc body shown in Fig. 3.

The next set of results displayed in Fig. 5 are for a similar shape, but with the maximum diameter located at $x = 0.70$. The ordinates for this shape are given by

$$R = A[x - x^n] \tag{17}$$

with $n = 6.03$ and A given by Eq. (16). Again the C_{pm}-input theoretical predictions are in very good agreement with the data. The free-air results indicate, however, as may have been

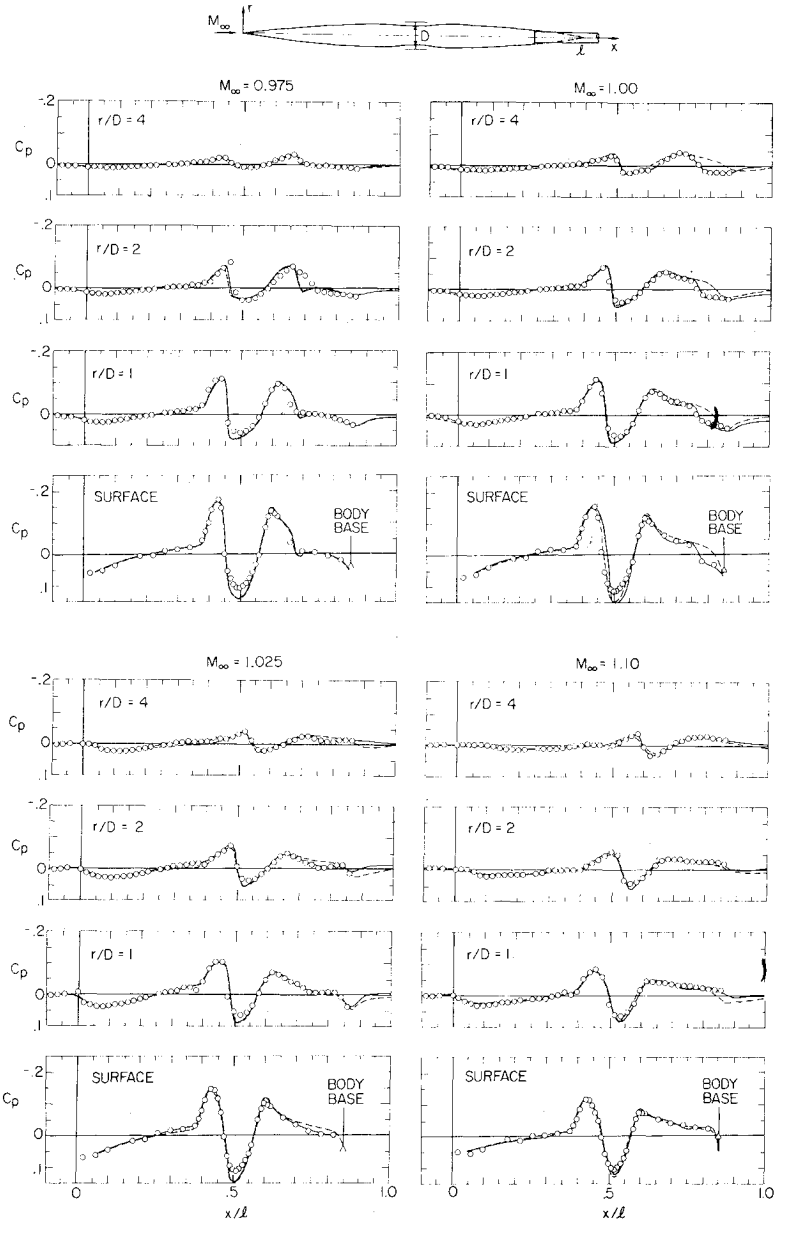

Fig. 7 Experimental[21] (○, □), and theoretical (-----) pressure distributions for an indented parabolic-arc body with $D/\ell = 1/14$ at several transonic Mach numbers; —C_{pm} ($r/D = 4$) input, --- free air.

anticipated from the comparisons given in Figs. 3 and 4, that tunnel interference for this shape is very small, and restricted essentially to the $M_\infty = 1.00$ results at axial locations behind $x = 0.90$.

Bumpy and Indented Bodies

In order to provide an indication of the ability of the method to handle situations where multiple shocks or several high-gradient regions exist on the control surface, we have examined the bumpy and indented bodies[21] which were also tested transonically in the Ames 14-ft wind tunnel. These bodies were quite long ($\ell = 112$ in.), and consisted of basic parabolic-arc bodies having maximum diameter to length ratios $D/\ell = 1/14$, but with a sinusoidal bump or indentation centered about the body midpoint and extending over $0.393 \le x \le 0.607$. The ordinates of the shapes are given by

$$R = (2D/\ell)(x - x^2) \pm \left(\frac{D}{10\ell}\right)\sin^2\left[\frac{\pi(x - x_1)}{(x_2 - x_1)}\right] \qquad (18)$$

where $(x_1, x_2) = (0.393, 0.607)$.

The results indicated in Fig. 6 are for the bumpy body. In the SLOR calculation of these results, as well as the indented-body results to follow, the same r-grid used for the smooth body results given in Figs. 3-5 was employed. The x-grid was refined by clustering 40 equally spaced points between $0.3 \le x \le 0.7$, and then using 30 geometrically-expanded points with grid ratio 1.2:1 to cover each of the regions $-2.0 \le x \le 0.3$ and $0.7 \le x \le 3.0$.

With regard to the results indicated in Fig. 6, the experimental flowfield pressures at the radial location $r/D = 4$—the outermost station at which data were taken—display much steeper gradients than any of the smooth body data shown in Figs. 3-5. In addition, the data at $M_\infty = 1.025$ and 1.10 indicate multiple regions of rapid compression. Comparison with the theoretical C_{pm}-input results displays very good agreement at all the Mach numbers. Some quite minor discrepancies are evident in the region behind the bump where boundary-layer/shock-wave interaction effects may have occurred. The free-air results indicate that tunnel interference exists for this shape at all the Mach numbers shown, with the strongest interference again at $M_\infty = 1.00$ and 1.025.

The corresponding indented-body results displayed in Fig. 7, on the other hand, show a very small tunnel effect at every freestream Mach number other than $M_\infty = 1.00$. Apparently, the body indentation significantly reduces the size and

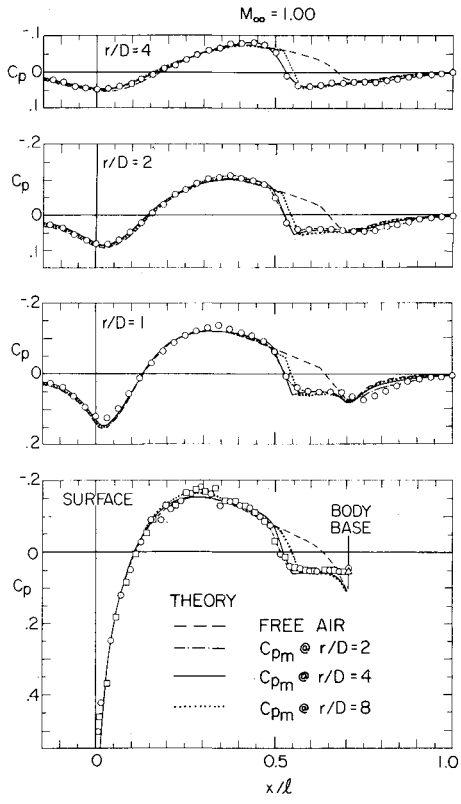

Fig. 8 Effect of control surface location on near-flowfield and body-surface theoretical pressure distributions at $M_\infty = 1.00$ for the $(x/\ell)R_{max} = 0.3$ body shape.

strength of the supersonic pockets for $M_\infty < 1$, and, similarly, the subsonic pockets at $M_\infty > 1$. In fact, at $M_\infty = 1.025$ and 1.10, the flow at $r/D = 4$ is purely supersonic. We note that, for all of the cases shown, the theoretical results for both free air and C_{pm} input indicate a higher pressure peak at the body midpoint than the data. This is undoubtedly due to a thickened boundary layer in the indented region caused by the decelerating flow. This effectively results in a shallower and milder indentation and consequent smaller pressure peak.

Effect of Control Surface Location

The final results shown in Fig. 8 display the effect of the predicted surface and near-flowfield pressures of varying the radial location of the control surface at which the experimentally measured boundary condition is imposed. These results are for the $(x)_{R_{max}} = 30\%$ body at $M_\infty = 1.00$, for which comparisons were previously shown in Fig. 4. This example was purposely selected for its strong tunnel-interference characteristics, as well as the fact that experimental flowfield pressures were obtained for this flow out to the radial location $r/D = 8$. The dashed and solid lines in Fig. 8 correspond as before to theoretical results for free-air and C_{pm} input at $r/D = 4$. The dash-dot and dotted lines correspond to theoretical results for C_{pm} input at $r/D = 2$ and 8. For the results with C_{pm} input at $r/D = 2$, the predicted pressures on the body surface and at $r/D = 1$ are essentially indistinguishable from the data everywhere, particularly in the vicinity of the shock wave. The C_{pm} input at $r/D = 4$ results are also quite satisfactory and differ but slightly from the $r/D = 2$ results only near the shock. For the C_{pm} input at $r/D = 8$, a consistent discrepancy in the shock positions for both the surface and flowfield pressures that amounts to approximately 3-4% of body length is observed, however. The flow-survey location at $r/D = 8$ is slightly more than halfway (4/7 H/ℓ) from the tunnel centerline to the closest point on the tunnel walls. For these results, it is likely that the nonaxisymmetric effects of the square-tunnel configuration are the cause of the discrepancy. If the tunnel cross section were cylindrical, the radial location of the control surface could probably be taken closer to the wall without loss of accuracy to the interior calculation. The important point of these results, however, is they demonstrate that for any test model/tunnel configuration there will always exist a minimum distance from the tunnel walls, closer than which it is inappropriate to obtain outer boundary data. Within that minimum distance from the wall, factors such as tunnel flow nonuniformities, local wall disturbances, etc., will tend to wash out the accuracy of the experimental measurements with a subsequent detrimental effect on the theoretical calculations.

Potential Utility

The ultimate utility of any interference assessment procedure is in the evaluation and reinterpretation of data obtained in a wind tunnel to corresponding free-air conditions. Toward that end, there are several interesting options in which the present procedure can be used. For the results reported, we have employed the assessment procedure primarily for the observation of two separate effects present in the data; viz., nonpotential effects of viscosity and rotation, and wind-tunnel interference. Nonpotential effects were evaluated by noting the difference between the data and the theoretical prediction with C_{pm} input, while the difference between the theoretical free-air calculation and that with C_{pm} input provided a measure of the tunnel interference present. While these two calculations in themselves do not reinterpret the data to free-air conditions, they serve to identify the range of test conditions where tunnel interference is minimum for a specific test article. Such information is of major importance for existing conventional transonic tunnels where wall control is limited or impossible, and relates to "the principle of minimizing interference rather than corrections."[23]

For the actual correction or reinterpretation of the test data to free-air conditions, Kemp[14] has suggested an iterative procedure which effectively corrects the tunnel data through corrections to the oncoming uniform flow. As related to the present axisymmetric problem, the first step of that method consists of solving the potential flow problem using experimentally measured pressures on both the control surface and the body, together with an imposed constraint employing measured drag. This calculation yields the potential solution for the tunnel flow, and, in particular, provides the effective potential-body shape. That shape is then used in an iterative series of free-air computations in which the oncoming Mach number is sequentially adjusted so that the resulting free-air flow is a "best" representation of the tunnel flow. For two- or three-dimensional lifting flows, constraints on measured lateral forces and corrections to the oncoming flow direction would enter the procedure as well.

Concluding Remarks

An evaluation has been made of a wind-tunnel interference assessment concept which employs an experimentally measured pressure distribution obtained along a convenient control surface as an outer boundary condition, together with an inviscid body-surface boundary condition. Based on the axisymmetric transonic small-disturbance equation, extensive calculations have been made for a number of slender bodies at Mach numbers in the transonic regime. Particular emphasis was placed on flows with oncoming Mach numbers at and near one, where tunnel interference was high and where the experimentally measured conditions on the control surface were of mixed subsonic/supersonic character. For all of these cases studied, the implementation of the measured boundary condition in Dirichlet form in the numerical procedure proved stable and no convergence problems were encountered. The predicted body-surface and near-flowfield pressure results have been compared with data and corresponding theoretical

free-air calculations. The comparisons with data display very good agreement, capturing the location and strengths of surface and flowfield shocks; while the free-air comparisons provide the basis for a quantitative evaluation of wind-tunnel interference. From these results, we conclude that such a procedure can be useful as a practical wall-correction method for moderately variable or fixed-geometry transonic wind tunnels where alteration of the tunnel walls is limited or impossible.

Acknowledgment

The results reported are based on research partially supported by the Air Force Office of Scientific Research under Contract No. F44620-75-C-0047 and by the U.S. Army Research Office under Contract No. DAAG29-77-C-0038.

References

[1] Baldwin, B., Turner, J., and Knechtel, E., "Wall Interference in Wind Tunnels with Slotted and Porous Boundaries at Subsonic Speeds," NASA TN 3176, 1954.

[2] Bailey, F. R., "Numerical Calculation of Transonic Flow about Slender Bodies of Revolution," NASA TN D-6582, 1971.

[3] Murman, E. M., "Computation of Wall Effects in Ventilated Transonic Wind Tunnels," AIAA Paper 72-1007, Sept. 1972.

[4] "Report of the AGARD Ad Hoc Committee on Engine Airplane Interference and Wall Corrections in Transonic Wind Tunnel Tests," AGARD-AR-36-71, Aug. 1971.

[5] Berndt, S. B., "Inviscid Theory of Wall Interference in Slotted Test Sections," ICAS Paper 76-03, Oct. 1976.

[6] Chew, W. L., "Cross-Flow Calibration at Transonic Speeds of Fourteen Perforated Plates with Round Holes and Airflow Parallel to the Plates," AEDC-TR-54-65, July 1955.

[7] Vidal, R. J., Erickson, Jr., J. C., and Catlin, P. A., "Experiments with a Self-Correcting Wind Tunnel," AGARD-CP-174, *Wind Tunnel Design and Testing Techniques*, Oct. 1975, pp. 11-1–11-13.

[8] Kacprzynski, J. J., "Transonic Flow Field Past 2-D Airfoils Between Porous Wind Tunnel Walls with Nonlinear Characteristics," AIAA Paper 75-81, Jan. 1975.

[9] Ferri, A. and Baronti, P., "A Method for Transonic Wind Tunnel Corrections," *AIAA Journal*, Vol. 11, Jan. 1973, pp. 63-66.

[10] Sears, W. R., "Self Correcting Wind Tunnels," *The Aeronautical Journal*, Vol. 78, No. 758/759, Feb./Mar. 1974, pp. 80-89.

[11] Chevallier, J. P., "Soufflerie Transsonique a Parois—Adaptables," AGARD CP-174, Oct. 1975, pp. 12-1–12-8.

[12] Goodyer, M. J., "A Low Speed Self Streamlining Wind Tunnel," AGARD CP-174, Oct. 1975, pp. 13-1–13-8.

[13] Sears, W. R., Vidal, R. J., Erickson, J. C., and Ritter, A., "Interference-Free Wind Tunnel Flows by Adaptive-Wall Technology," ICAS Paper 76-02, Oct. 1978.

[14] Kemp, Jr., W. B., "Toward the Correctable-Interference Transonic Wind Tunnel," *Proceedings of AIAA 9th Aerodynamic Testing Conference*, June 1976, pp. 31-38.

[15] Krupp, J. A. and Murman, E. M., "Computation of Transonic Flows Past Lifting Airfoils and Slender Bodies," *AIAA Journal*, Vol. 10, July 1972, pp. 880-886.

[16] Guderley, K. G., *The Theory of Transonic Flow*, Pergamon Press, Mass., 1962.

[17] Cheng, H. K. and Hafez, M. M., "On Three-Dimensional Structure of Transonic Flows," USCAE 121, July 1972.

[18] Murman, E. M., "Analysis of Embedded Shock Waves Calculated by Relaxation Methods," *AIAA Journal*, Vol. 12, May 1974, pp. 626-633.

[19] Jameson, A., "Transonic Flow Calculation," Lecture Series 87, von Karman Institute for Fluid Dynamics, Computational Fluid Dynamics, March 1976.

[20] McDevitt, J. B. and Taylor, R. A., "Pressure Distributions at Transonic Speeds for Slender Bodies Having Various Axial Locations of Maximum Diameter," NACA TN 4280, 1958.

[21] Taylor, R. A., "Pressure Distribution at Transonic Speeds for Bumpy and Indented Midsections of a Basic Parabolic-Arc Body," NASA Memo 1-22-59A, 1959.

[22] Spreiter, J. R., Smith, D. W., and Hyett, B. J., "A Study of the Simulation of Flow with Free Stream Mach Number 1 in a Choked Wind Tunnel," NACA TR R-73, 1960.

[23] Berndt, S. B., "On the Influence of Wall Boundary Layers in Closed Transonic Test Sections," FFA Rept. 71, 1957.